

On the Application Potential of Chemically Tailored Metal Oxide and Higher Chalcogenide Nanoparticles for Nanoscale Resistive Switching Devices

Anne Frommelius, Thorsten Ohlerth, Michael Noyong, and Ulrich Simon*

Resistive switching (RS) for nonvolatile data storage is a highly relevant field of research. Up to now, RS devices are fabricated via semiconductor processing technologies. This poses the question of whether integration of chemically tailored nanoparticles, either consisting of valence change or phase change materials, can be integrated in nanoelectrode configurations in order to explore their functionality for RS applications. This review discusses the RS properties of such nanoparticles by means of selected examples of both nanoparticle assemblies as well as on the individual particle level. Although this field of research is rather unexplored, it becomes evident that chemically tailored nanoparticles bear great potential for RS applications.

With respect to electronic applications, particularly metal, and metal oxide NPs have been investigated for a plethora of different technical uses, including gas sensing,^[10] printed electronics,^[11] or photovoltaics,^[12] just to name a few. However, most of these applications utilize the electronic properties of ensembles of particles, rather than that of single ones. Hence, collective phenomena determine the overall electrical properties, and structural features, such as packing disorder or domain interfaces may dominate the integral behavior, rather than the tailored and unique features of the individual building blocks. As a consequence, many of these applications do not take advantage of


1. Introduction

The chemical synthesis of inorganic nanoparticles (NPs), which show size-dependent physico-chemical properties, has evolved to a prosperous research field and has meanwhile found its way to many different areas of applications, including energy storage,^[1] catalysis,^[2] photonics,^[3] or electronics.^[4–9] In many cases, such NPs can be synthesized via likewise easy-to-handle liquid-based colloid-chemical routes with a high degree of control over nucleation, growth, and shape evolution. In order to prevent such particles in solution from agglomeration and further growth, they need to be stabilized, either by introducing a surface charge through ionic additives or by organic molecules, so called capping ligands or surfactants. Such molecules enable either for steric or for electrostatic colloidal stabilization, or for combinations of these, and they allow for liquid phase processing.

the minute size of the NPs and thus do not fully utilize the size-dependent properties that arise from the 3D confined electronic and structural state of the NPs what would enable a leap toward further miniaturization.

The electrical properties of individual particles are typically studied by means of microscopic techniques, such as scanning tunneling microscopy or conductive atomic force microscopy (c-AFM).^[13] These techniques provide detailed insights into the electronic structure and electronic transport phenomena. However, they are less suited for building up devices that utilize the individual particles properties for a desired application. This can meanwhile be achieved by integrating individual metal NP into nanoelectrode configurations, which are compatible with CMOS technology and semiconductor processing. Hence, two-terminal cells can be fabricated, where the metal NP serves as a metallic island surrounded by the organic ligand shell. Thereby, the ligand shell represents more than just a “dielectric spacer” in a typical electrode–insulator–NP–insulator–electrode configuration. It has been shown that breaking the symmetry by anisotropic arrangements of the ligands on the NP surface, i.e., by forming “patchy” or “Janus-type” particles, allows for directionality in binding. This, in turn, allows for directionality in the electrical transport properties,^[14,15] which, e.g., has recently been described for Janus-type gold (Au) NPs in a heterometallic nanoelectrode configuration. It was demonstrated that rectifying current–voltage characteristics have been achieved by functionalizing the Au NPs with molecules bearing different intrinsic electronic properties and different functional terminal groups on the opposite hemispheres. In this configuration, the terminal groups enabled the directed immobilization between heterometallic nanoelectrodes and the charge transport through the resulting device revealed the characteristics of both types of molecules, forming an asymmetric double

A. Frommelius, T. Ohlerth, M. Noyong, U. Simon
RWTH Aachen University
Institute of Inorganic Chemistry
Landoltweg 1 a, 52074 Aachen, Germany
E-mail: ulrich.simon@ac.rwth-aachen.de

 The ORCID identification number(s) for the author(s) of this article can be found under <https://doi.org/10.1002/pssa.202300456>.

© 2023 The Authors. physica status solidi (a) applications and materials science published by Wiley-VCH GmbH. This is an open access article under the terms of the Creative Commons Attribution-NonCommercial-NoDerivs License, which permits use and distribution in any medium, provided the original work is properly cited, the use is non-commercial and no modifications or adaptations are made.

DOI: 10.1002/pssa.202300456

tunneling barrier. Hence, in such a configuration, the electrical functionality mainly depends on the distinct binding configuration between ligand and electrode as well as on the electrical transport properties of the ligand molecules, while the metal NP just serves as a metallic island with its size-dependent electrostatic charging energy.

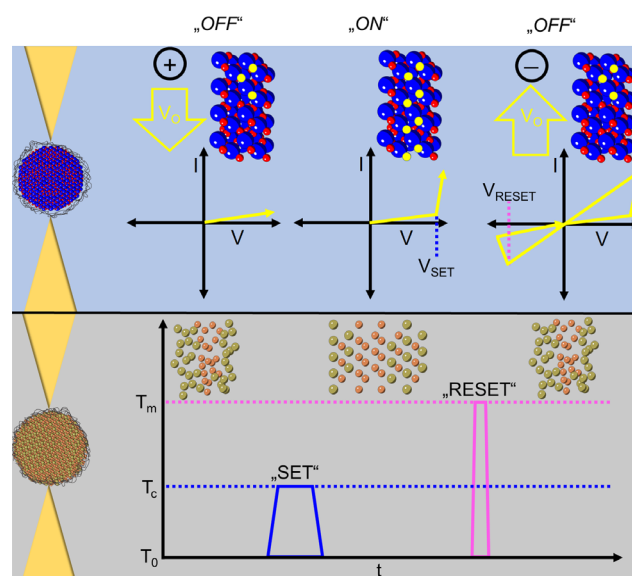
It would be highly desirable to integrate an additional functionality into the NP itself and to utilize this for a new level of device functionality, e.g., for resistive switching (RS) in non-volatile data storage. While RS phenomena on nanostructures fabricated via semiconductor processing technologies is a rather rapidly growing and technologically highly relevant field, such as in resistive random access memories (ReRAMs),^[16] attempts to integrate chemically designed NPs, that can undergo non-volatile resistance changes, in nanoelectrode configurations are rather unexplored and only first steps in this direction have been made. However, in order to take full advantage of the tunability of NPs' physical properties by tailoring their size, shape, and surface functionalization, integration of a controlled number of well-defined NPs into a nanoscale device concept would be key. Eventually, the resulting electrode–ligand–NP–ligand–electrode configuration as a two terminal cell would comprise both, the tailored ligand properties and the intrinsic properties of the central NP, and thus would open up new application scenarios that go beyond the current state of research.

RS includes a class of phenomena where the electrical resistance of a two-terminal cell comprising a metal–insulator–metal (MIM) architecture changes in a hysteretic manner upon an external electrical stimulus. Typically, the cell can be switched between a high-resistive state (HRS) and a low-resistive state (LRS), which represent the binary extremes, i.e., the “ON” and “OFF” states, while multiple resistance states are achievable as well by selecting appropriate stimuli, which further increases the application potential.

Among the manifold RS phenomena, this review will set its focus on two fundamentally different switching effects, i.e., valence change (VC) effects that are predominantly observed in metal oxides, and phase change (PC) effects that are mostly observed in higher metal chalcogenides. As there are many excellent and comprehensive reviews on RS, to which we would like to refer and which cover the different switching mechanisms observed so far,^[17–20] we will only give a very brief and simplified phenomenological description of the two phenomena.

The VC effect is typically triggered by a forming process that causes the formation of conducting paths or filaments along extended defects. The forming process as well as the switching effect itself induces a field-oriented local nanoionic redox reaction, which is facilitated by a migration of oxygen ions or charged defects, see **Scheme 1**. The resulting change in local stoichiometry causes a VC of the cation sublattice, leading to a change in the electrical resistance. This effect is typically restricted to the electrode–oxide interface.

The PC effect utilizes the difference in electrical resistivity between the high-resistive amorphous phase and a low-resistive crystalline phase of various higher chalcogenides and even in mono-elemental systems. The switching between the LRS and the HRS is achieved by local melting and quenching of the respective material by a short, strong current pulse leading to amorphization, while the way back to the LRS by partial recrystallization results from Joule heating induced by a longer, but



Scheme 1. Schematic illustration of the integration of VC NP (top) and PC NP (bottom) into a nanoelectrode configuration and structural changes that are induced by the applied voltage causing switching. For VC materials, the applied voltage causes the migration of oxygen vacancies (V_O , represented as yellow spheres) that reversibly transforms the materials from a HRS (i.e., “OFF”) into the LRS (i.e., “ON”). For this, according set (V_{SET}) or reset (V_{RESET}) pulses have to be applied. For PC materials, V_{SET} transforms the material from an amorphized HRS to a crystalline LRS. V_{RESET} , followed by rapid thermal quenching, re-amorphizes the structure and leads back to the HRS.

weaker, current pulse. While there is ongoing debate about the specific binding configuration in PC materials, the PC effect is accompanied by local rearrangements of the atoms as well as changes of the electron densities in the chemical bonds.^[21]

By means of selected examples, this review will illustrate recent attempts to evaluate metal oxide and higher chalcogenide particles as possible building blocks for nanoscale RS. We will cover examples of NP assemblies applied as compact films, NPs embedded in a polymer matrix, NPs in monolayers, and we will showcase switching experiments on individual NPs. Thereby we intend to highlight the most relevant developments achieved so far, whereas we will put some emphasis on our own work of the last decade.

2. Metal Oxide Nanoparticles in Valence Change Settings

2.1. Surfactant-Free Fabrication Methods

There have been several approaches that integrate solution-processed metal oxide NP as a formal insulating layer within the MIM architecture. In terms of NP assemblies, Kim et al. were among the first groups to integrate magnetite (Fe_3O_4) NPs as resistive material into an RS device.^[22] The NPs are obtained in different sizes (diameters of 7, 9, 12, and 15 nm), and they were compressed to a pellet with sizes of $0.5 \cdot 1 \cdot 4 \text{ mm}^3$ after organic surfactants ligands were removed chemically. These rather thick assemblies of magnetite NPs showed bipolar RS features with an R_{OFF}/R_{ON} ratio of ≈ 20 . Accordingly, switching

behavior could be extended to related spinel structures, such as MnFe_2O_4 . Later, it was shown that by repetitively dip-coating electrodes into organic colloidal dispersions of maghemite NPs, thin films of about 300 nm can be established, see **Figure 1**.^[23,24] As mentioned in the introduction, for this approach, it is unavoidable to functionalize the surfaces of the NPs. This is why after each dip-coating a subsequential sintering step needs to be performed, so that the surfactants are removed. Another beneficial aspect of the sintering is that the particles

coalesce and form a mechanically stable contact with the electrode and thereby provide several percolation paths.

In **Figure 1c**, the I - V characteristics of $\text{Al}/\gamma\text{-Fe}_2\text{O}_3$ NP multilayer/ Al -plate structure exhibit multilevel RS, with the resistance decreasing at higher voltages and switching not observed at ± 6 V. These results suggest a possible RS mechanism where multiple conducting filaments are reversibly formed and ruptured, potentially due to a phase transition of NPs from $\gamma\text{-Fe}_2\text{O}_3$ to Fe_3O_4 . The RS could be associated with nanoscale redistribution of atoms or vacancies within the $\gamma\text{-Fe}_2\text{O}_3$ NP assembly, with the large volume of voids between NPs facilitating this redistribution.

Furthermore, these assemblies have an extremely porous structure. The resulting enhanced surface area is concomitant with a higher concentration of potential ionic defects, i.e., oxygen vacancies (V_O). Thus, it is worth mentioning that the inherent characteristics and behaviors of NP-layered thin-film assemblies exhibit significant differences when compared to those thin films produced through top-down processing methods. Thereby, it is important to note that this does not necessarily involve a different redox chemistry of the insulating material. In the here described example, the formation of a conducting filament in thin films can be observed as an abrupt increase of conductance, while the pathways in the NP-based structure are gradually increased by applying voltage repetitively. The corresponding switching behavior can be interpreted as a space charge limited current (SCLC) conduction mechanism; this is demonstrated in the I - V curve's linear relationship in a log-log scale, showing ohmic resistivity at low voltages (below around 4 V) where the injected current density is less than thermally generated carrier density, and a transition to SCLC conduction as the voltage increases (up to about 8 V).^[23] Other conduction mechanisms, like Schottky emission, tunneling, or Poole-Frenkel conduction, were excluded as the current is likely to flow through the filaments by SCLC conduction due to the high density of interface trap sites. There are more fundamental explanations and controversies for different types of conduction or "leakage currents," which are assumed for MIM stacks and how the current is either interface controlled by means of thermionic field emission and tunneling carrier injection or the current is bulk controlled through SCLC or the Poole-Frenkel effect.^[25] However, this discussion goes well beyond the scope of this review. Yet, in terms of NP assemblies, it is noteworthy that the increased interface area promotes the electron transport via a high concentration of trap sites, so the SCLC is affected by this tremendously. As a consequence, increasing pulse voltages and widths not only allow for RS but also gradually increase the resistance bias between the LRS and HRS. Such analog-type switching (see **Figure 1c**) is different from the corresponding thin-film structures and enable the potential to simulate novel approaches such as neuromorphic devices.^[26,27] However, high voltage or current application may not always form filaments, as both, formation and rupture are influenced by concentrated electrical fields that lead to inconsistent switching characteristics. To improve uniformity and scalability in further miniaturized devices, it would be necessary to control RS within single or few NPs or nanowires (NW) and further investigate the impact of assembly thickness and lateral size on multilevel switching uniformity.

Concerning thinner assemblies, Younis et al. used CeO_2 nanocubes (NC) with side lengths of 5 nm and created ≈ 163 nm-thick

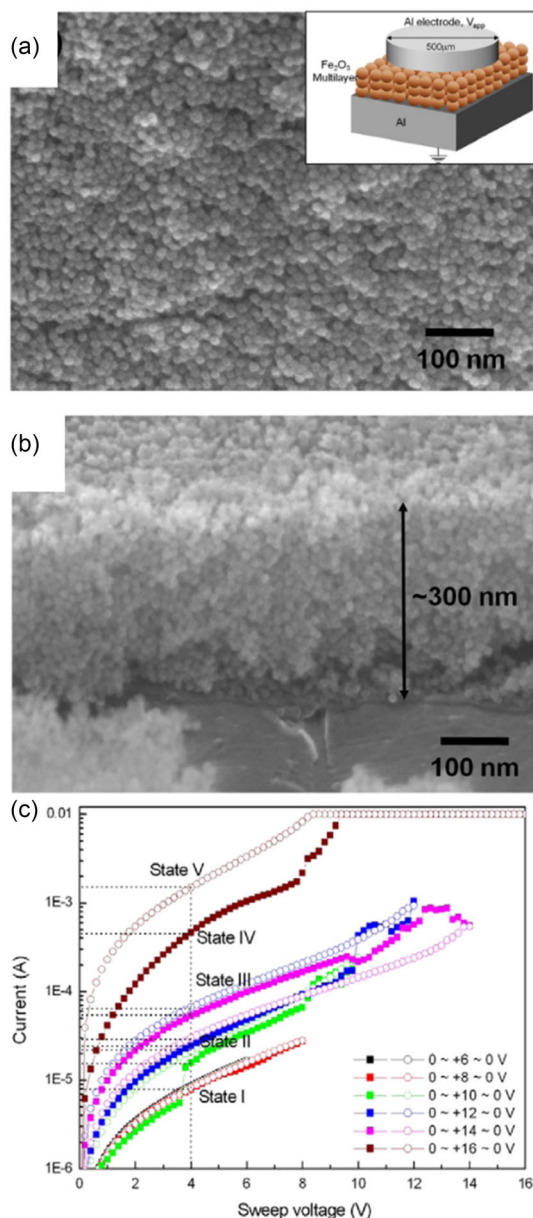


Figure 1. a) Plan-view and b) oblique-angle view SEM micrographs of $\gamma\text{-Fe}_2\text{O}_3$ NP multilayer on Al plate formed by repeating dip coating and annealing steps ten times (inset: schematic of $\text{Al}/\gamma\text{-Fe}_2\text{O}_3$ NP multilayer/ Al -plate structure). c) I - V characteristics of $\text{Al}/\gamma\text{-Fe}_2\text{O}_3$ NP multilayer/ Al -plate structure at the different voltage sweep ranges; ± 6 and ± 8 V, ± 10 and ± 12 V, ± 14 and ± 16 V in the positive voltage range. Adapted with permission.^[23] Copyright 2011, IOP Publishing Ltd.

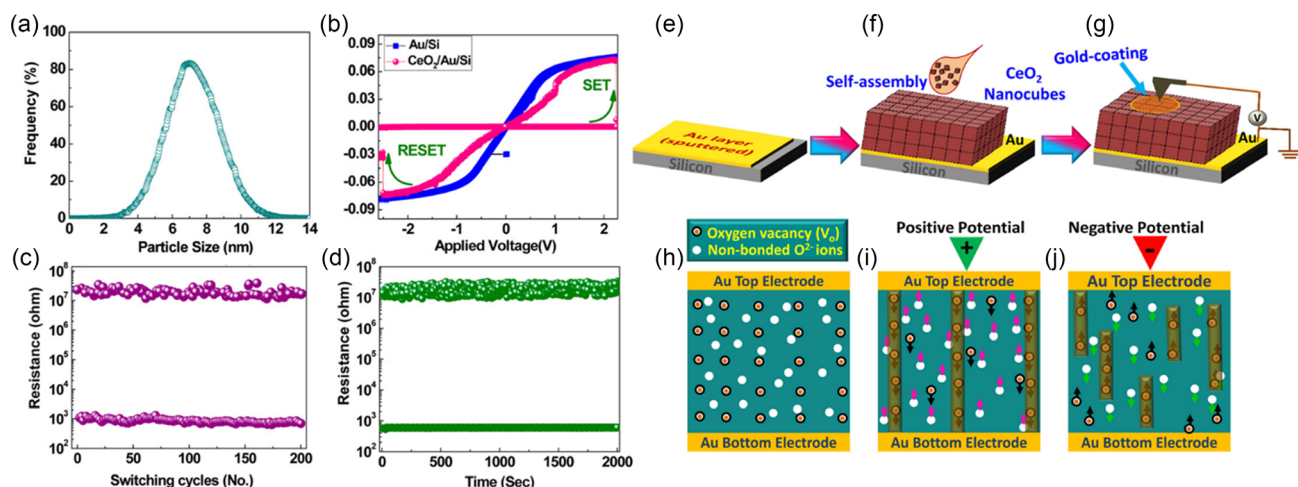


Figure 2. a) Particle-size distributions of the CeO_2 nanocubes. b) I - V measurements on the linear scale. c) Endurance performance of the device for 200 switching cycles. d) Data retention performance of the device for 2000 s. e and f) Schematic diagram for the self-assembly of CeO_2 nanocubes to form an RS device. g) Setup for I - V measurements. Schematic model demonstrating the conduction process in the device h) without potential, i) with positive potential, and j) with negative potential. Adapted with permission.^[23] Copyright 2013 American Chemical Society.

assemblies of by threefold dip-coating gold electrodes into the nanoparticle dispersion, see **Figure 2**.^[28] The CeO_2 NC were similarly processed by sintering and the counter electrode was sputtered on top of the NP layers. $R_{\text{OFF}}/R_{\text{ON}}$ ratios of 10^4 were achieved with thermal stability of up to 200°C with more than 10^2 cycles (cf. Figure 2b–d). The authors note that thinner films exhibit lower $R_{\text{OFF}}/R_{\text{ON}}$ ratios due to a deficit in V_{O} , which are essentially charge carriers. In contrast, for thicker films, they have demonstrated an uptick in charge carrier density by means of Hall effect measurements. However, the corresponding lower $R_{\text{OFF}}/R_{\text{ON}}$ ratios for these thicker films, specifically those exceeding 163 nm, are found to be smaller compared to devices with relatively thinner films. This is attributed to the necessity of applying higher effective field strengths to generate charge carriers via redox reaction processes. The authors propose an RS mechanism model that shares similarities with the widely accepted filamentary growth mechanism previously mentioned. In this model, V_{O} or free oxygen ions (O^{2-}) play the role of charge carriers.^[28]

The initial state has a high resistance, which is not only due to the NC bulk but also the interfaces between the particles that act as barrier (h). Upon applying a positive potential, O^{2-} are attracted toward the anode and are likely to form a reservoir at the electrode/ CeO_2 interface (i). When the oxygen vacancy density is high enough, percolation paths between the filament are formed that enable electrons to tunnel through the potential barrier, so the system is in the LRS. The opposite voltage immediately interrupts these conductive paths by pushing the V_{O} away from the cathode, resetting the device to the HRS (j). Compared to polycrystalline films in analog tests, these CeO_2 showcased a generally much higher resistance ($10^7 \Omega$) than their thin-film counter parts ($<10^3 \Omega$), which effectively results in a higher and more desirable high $R_{\text{OFF}}/R_{\text{ON}}$ ratio.

Despite the differences between common thin films and assembled NP as insulating material in a MIM structure, NP can form structures that are not only confined in one, but in all three dimensions. This motivated other groups to integrate

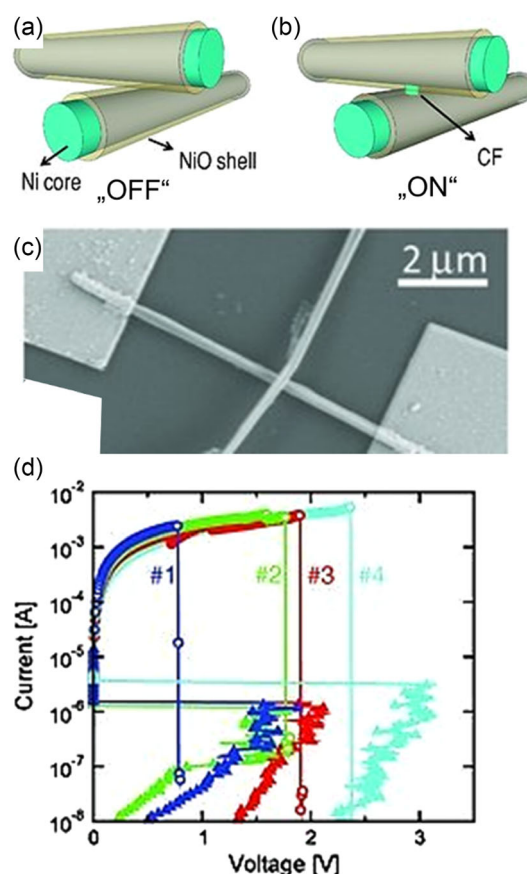


Figure 3. Schematic illustration of the crossbar memory structure formed from two NiO–Ni core–shell NWs in HRS a) and LRS b), differing by the presence of a conducting filament, and the consequent I - V curves. c) Hybrid bottom-up/top-down crossbar structures between a core–shell NW and corresponding measured I - V d) curves showing SET/RESET for four sequential cycles. Adapted with permission.^[31] Copyright 2011 WILEY-VCH Verlag GmbH & Co. KGaA, Weinheim.

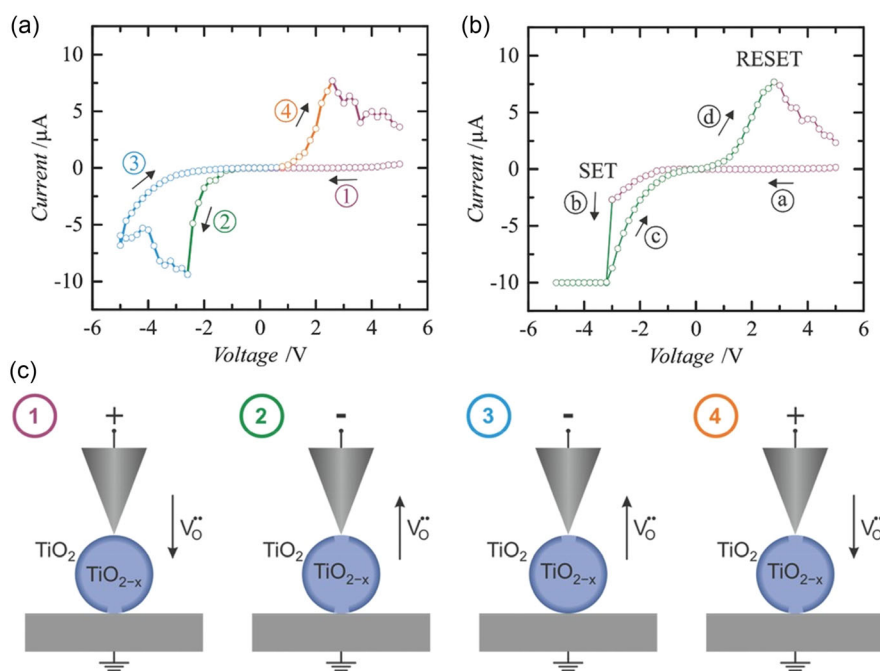


Figure 4. Exemplary I - V curves showing a) CS-type and b) BS-type behavior of $[\text{Pt}/\text{Ir}]/\text{TiO}_{2-x}$ NP/ $[\text{Pt}/\text{Ir}]$ devices. c) Schematic illustration of different steps “1” to “4” during the CS process in a vacuum-annealed TiO_{2-x} NP with an assumed core-shell-like structure. Reproduced with permission.^[32] Copyright 2015 WILEY-VCH Verlag GmbH & Co. KGaA, Weinheim.

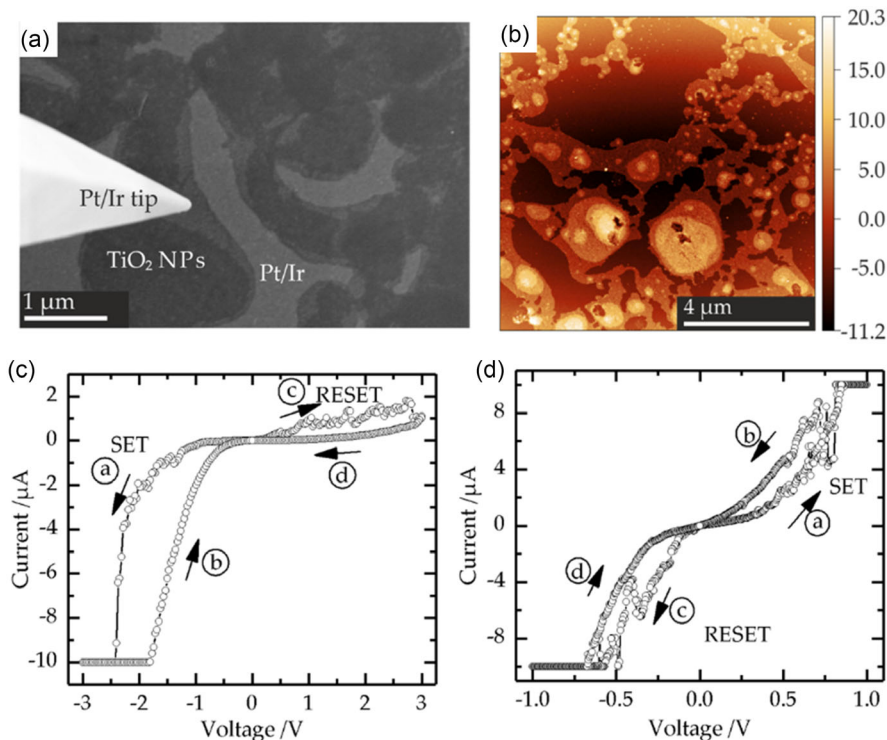


Figure 5. Exemplary SEM image of a TiO_2 NP film on the Pt/Ir surface transferred by the one-step method; on the left-hand side, the Pt/Ir-coated tip electrode is visible a) and tapping mode AFM image of the TiO_2 NP film transferred by the microcontact printing method onto a Pt/Ir surface b). Two I - V curves recorded on different TiO_2 NP monolayers exhibiting BS behavior c,d) (arrows and small letters depict voltage sweep sequence). Adapted with permission.^[34] Copyright © 2017 MDPI.

individual NPs into an electronic device and elucidate the RS mechanism where the effect of dimensional confinement comes into play.^[29] One elegant way was established by using Ni-based NW. In one of these studies, the NW are composed of a core-shell structure: a metallic Ni core that acts as connection for electrodes in the crossbar-like device set-up and an insulating NiO shell that constitutes the active switching layer during the voltage sweeps (see **Figure 3a–c**).^[30,31]

In this way, RS of two perpendicularly stacked Ni/NiO–NW with a total diameter of 200 nm (with an ≈ 15 nm-thick oxide layer shell) was shown. The change in resistance could be unambiguously assigned to the crossing junction of the two NW. It is therefore reasonable to assume that a conductive filament is generated by means of local reduction of NiO at this cross junction (**Figure 3a,b**). The $R_{\text{OFF}}/R_{\text{ON}}$ ratios of about 10^5 are comparable with planar NiO devices. It was also shown that cycle stability was limited to only four ON/OFF switching cycles, which is probably due to mechanical failure caused by thermally induced mechanical stress of the crossbar construction (**Figure 3c,d**). However, these findings serve as a proof of concept for NW-based crossbar memories. These NW-based RS devices were discussed in depth by Ielmini and coworkers. Their and other studies show that core-shell NiO–Ni NWs can act as flexible building blocks with inherent high scalability for high-density crossbar memory arrays.^[30,31]

In the context of this review, it should be noted that these NW were synthesized through electroplating. In that regard, Schmidt et al. could transfer the core-shell phenomenon from the NiO-based NW toward chemically synthesized TiO_{2-x} NPs.^[32] These NPs with a size of 80 nm in diameter showcase not only a bipolar

switching (BS) behavior, but predominantly a complementary switching (CS) mechanism (see **Figure 4a,b**).

A nanorobotics setup installed in a scanning electron microscope (SEM)^[33] was used to electrically address individual NPs via a conductive tip electrode and bottom electrode. Both electrodes were coated with a [Pt/Ir] film so that in the end a [Pt/Ir]/ TiO_{2-x} -NP/[Pt/Ir] configuration was formed. The switching model is explained in **Figure 4c**. Starting with a high voltage of +5 V at the tip, the already oxidized TiO_2 shell of the NP accumulates O^{2-} ions that further insulate the tip–NP interface. On the other hand, the local shell at the interface between the bottom electrode and the NP has a high concentration of V_O , which makes it an ohmic contact, but due to the insulating tip–NP interface, the configuration is overall in the HRS. When the polarity of the tip is turned to voltage of –2.5 V, the insulating shell of the tip–NP is destroyed, which leads to a voltage drop and an increase of the current. At this point, the configuration is switched to the LRS. A further decrease of voltage leads to the oxidation of the bottom electrode and NP interface, so the configuration is switched back to the HRS in the same polarity, which is typical for the CS mechanism. Still, some NPs exhibit BS mechanism or even show a transition from the CS to the BS mechanism. For that, one of the electrode–NP interfaces remain in the oxygen deficient and thus conducting state. Given that the atmosphere within the SEM is at 10^{-6} mbar and gaseous oxygen is released at the electrodes, it is hypothesized that the

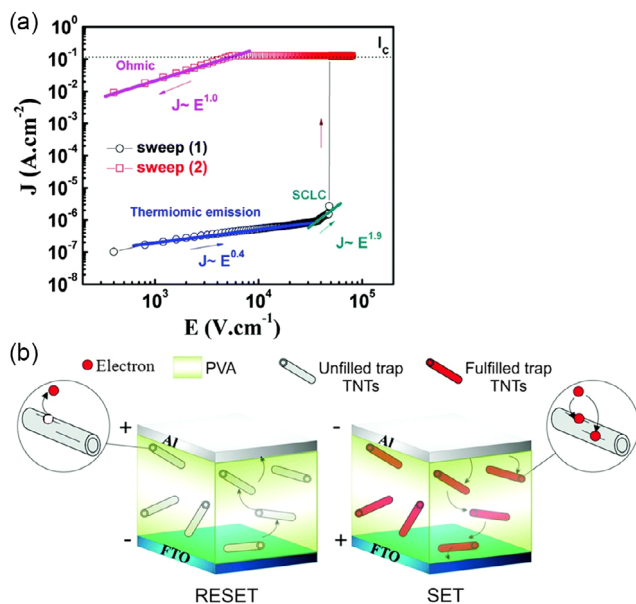


Figure 6. a) Current density–electric field strength (J – E) plot of current transport mechanism of the Al/PVA:TNTs/FTO device (FTO = fluorine-doped tin oxide). b) Schematics of the charge trapping–detrapping process in the Al/PVA:TNTs/FTO device corresponding to the SET and RESET process of RS behavior. Reproduced with permission.^[39] Copyright © 2018 Royal Society of Chemistry.

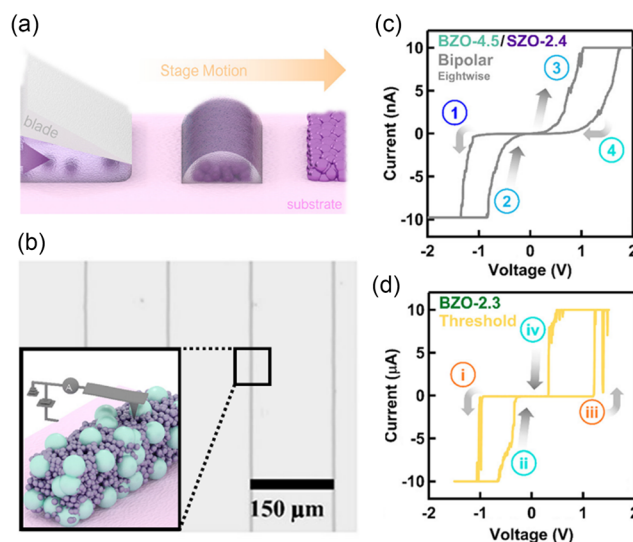


Figure 7. a) NP solutions are injected under a blade against a rigid substrate, where “stop-and-go” motion of the stage produces NP ribbon assemblies to form, as shown in b), an optical micrograph of BZO-4.5 NP ribbon assembly arrays. The insert shows a schematic illustration of the c -AFM measurement geometry across an individual polymodal nanoribbon assembly. c) I – V response of a BZO-4.5/SZO-2.4 polymodal nanoribbon (height = 80 nm) displaying “eightwise” BS character, as indicated by the arrow markers. Here “1” indicates the SET process, “2” and “3” indicate the LRS response, and “4” indicates the RESET process. d) I – V response of an individual BZO-2.3 monomodal nanoribbon displaying (volatile) threshold switching behavior. Here “i” and “iii” indicate the threshold voltage and increase to the LRS; “ii” and “iv” initiate the return to the LRS. Adapted with permission.^[82] Copyright © 2021 American Chemical Society.

reoxidation of the TiO_{2-x} interface might be prevented. Due to the high work functions of the cathodes there is no other oxygen source that could reincorporate O^{2-} ions back into the NP. This is in line with the observation that after several triangular voltage sweeps, the LRS remains intact, which indicates that at least one required insulation layer at the electrode–NP interface cannot be retrieved for either electrode anymore. This further supports the assumption that oxygen is extracted from the TiO_{2-x} -NP system.

Subsequent experiments by Schmidt et al. rendered to some extent the combination of both: a thin-film deposition and switching of individual sub-10 nm TiO_2 NPs.^[34] For this, the formation of multilayers, as discussed earlier, has to be prevented. Experiments with controlled water surface curvature enable in best-case scenarios the formation of monolayers of NPs (corresponding to a film thickness of ≈ 5 nm) which are transferred to the substrate surface that acts as bottom electrode, see **Figure 5**.

The different regions, i.e., NP monolayers or particle free electrode surfaces, could be identified by means of the aforementioned nanorobotic setup. For monolayers and multilayers, bipolar RS behavior was observed (Figure 5c,d). High voltage and current, possibly generating Joule heating, were seen to induce structural changes in a layer of TiO_2 NPs, potentially resulting in direct contact between the measurement tip and the Pt/Ir surface, thus causing observed ohmic behavior. Factors such as thermal drift and creep effects in the piezoelectric control elements might also lead to direct contact, and though most measurements showed a short circuit, it was hypothesized that individual sub-10 nm TiO_2 NPs might be reduced to more conductive Magnéli phases, leading to the observed switching behavior.^[34]

Eventually, a very recent research explores the properties of three-dimensionally confined HfO_2 nanoislands, grown by van der Waals epitaxy, with an eye toward their potential application in highly scaled ReRAM devices.^[35] Detailed analysis using scanning probe methods and ab initio simulations revealed the nanoislands' structural and electronic properties, which demonstrated characteristics similar to bulk material. Interesting findings include the presence of various acceptor- and donor-like in-gap states, suggesting a significant role for hafnium carbide formation and other defect states in the nanoislands' behavior. The identification of sub-nanometer HfO_2 crystals and a detailed understanding of their atomic structure provide new insights into the first nucleation steps in the formation of these nanostructures. Ultimately, van der Waals epitaxy requires an ultraflat substrate like graphene. This is where chemically synthesized NPs might have an edge, as they can be deposited on basically any material.

2.2. Influence of Organic Matrices in NP-Based ReRAM

Incorporating chemically synthesized NPs into a ReRAM device poses challenges not only in the assembly process but also due to the prevalence of organic capping agents. However, some groups have successfully used organic matrices as a dielectric component in a switching cell, effectively utilizing what was initially a disadvantage.^[36–39] One method involves creating a thin-film layer by spin-coating metal oxide NPs within a polyvinyl alcohol (PVA) as polymer.^[38–41] This composite mixture of metal oxide and polymer has demonstrated promising switching capabilities in recent years. The RS characteristics can be illustrated using a hybrid organic–inorganic device exhibiting BS behavior,

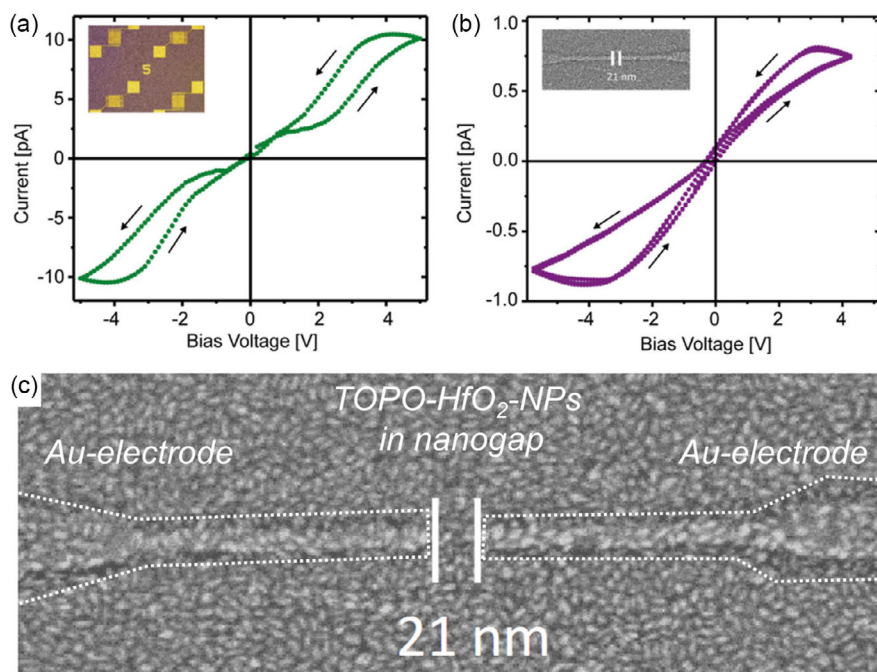


Figure 8. I - V curves of rod-like NP (dry) films recorded by periodic voltage sweeps in a) microelectrode device (channel width of $5\ \mu\text{m}$, sweep rate of $10\ \text{mV s}^{-1}$). Inset: microchannel device. b) Nanoelectrode device (nanoelectrode separation $21\ \text{nm}$, sweep rate $100\ \text{mV s}^{-1}$). Inset: SEM image of a nanoelectrode device with rod-like nanoparticles. c) Magnification of the inset in (b) highlighting the respective subunits. Adapted with permission.^[45] Copyright © 2022 American Chemical Society.

for instance with TiO₂ nanotubes and PVA.^[39] Notably, the materials—PVA polymer or TiO₂-nanotubes—do not show switching hysteresis individually.

The current transport mechanism in these composite materials involves an interface controlled thermionic emission mechanism, which injects charge carriers from the electrode into the polymer (**Figure 6**). Starting from a HRS, charge carriers are injected into the PVA polymer at low voltages. With increasing voltage, the system's conductivity is enhanced by trap-controlled SCLC and a charge transfer occurs between the polymer and the TiO₂-nanotubes, following a donor–acceptor mechanism. When all acceptor traps in the TiO₂-nanotubes are filled, the current spikes and the device switches to an LRS with ohmic behavior. The TiO₂ nanotubes thus serve as electron acceptors within an electron donor matrix. A reversed bias regenerates charge carrier traps within the NP, resetting the system to the HRS. These hybrid systems are stable in ambient conditions, inexpensive, easy to manufacture, mechanically robust, and flexible due to the polymer matrix. However, further studies are needed to understand the switching behavior concerning the polymer host matrix, temperature, and variations in nanofiller loading.^[41] Moreover, upscaling a spin coating process for industrial use remains challenging due to its treatment of small substrates, material waste, and difficulty achieving thin-film layer formations below 10 nm, a critical threshold in the semiconductor industry.

The group of Nonnenmann has shown the employment of HfO₂ NPs as nanoribbon-like thin films.^[42] They propose that the switching behavior correlates linearly with the length of the capping ligands they used for the colloidal stabilization of the NPs. Shorter ligands are thereby concomitant with an increased tunneling probability due to the shorter interparticle spacings. In another study, they solvothermally synthesized differently sized BaZrO₃ (BZO, 4.5 and 2.4 nm in diameter) and SrZrO₃ (SZO, 2.4 and 9.0 nm in diameter) NPs and stabilized those with 2-hexyldecylphosphonic acid as capping ligands.

The particles were assembled via a flow-coating method (see **Figure 7a**) and deposited onto a Pt substrate that acts as bottom electrode. The ribbon height was ≈80 nm. The authors found a BS response of NP nanoribbon assemblies using a sweeping voltage (see **Figure 7c**) applied to a Pt bottom electrode and collected by a grounded Pt top electrode. The voltage sweep starts with negative polarity, initially showing a HRS before reaching a V_{SET} that induces a significant increase in current and establishes an LRS. The LRS remains even after removing the applied voltage, proving the nonvolatile nature of the nanoribbons. Both “eightwise” and “counter-eightwise” hysteretic BS responses were observed for BZO and BZO/SZO nanoribbon assemblies. The coexistence of BS with opposite polarity trends is similar to SrTiO₃ and TiO₂ thin-film studies, which attribute the polarity conversion to local changes in defect density. Oxygen exchange at the Pt electrode interface affects local vacancy concentration and the migration of V_O, which in turn modulate the depletion region and barrier height. However, most nanoribbon assembly combinations exhibit threshold switching responses (see **Figure 7d**). The typical threshold response is similar to the bipolar response but differs in the behavior of the LRS. Unlike the nonvolatile bipolar response, where the LRS is maintained toward the maximum positive bias, the volatile threshold response returns to the HRS at zero bias and maintains the

HRS in the opposite polarity until the threshold bias is reached. Similarly to the NiO/Ni NW or the iron oxide NP thin films that were discussed above, other studies have shown that parameters like temperature, electrode thickness, current compliance, or oxygen stoichiometry can cause instabilities in oxide thin films, while in the case described here it results in a conversion from BS to threshold switching.^[43,44] The nanoribbon assemblies were measured at ambient temperature, indicating that temperature is not the cause for this transition. Although the nanoribbon systems do not exhibit filamentary-based switching, inefficient heat

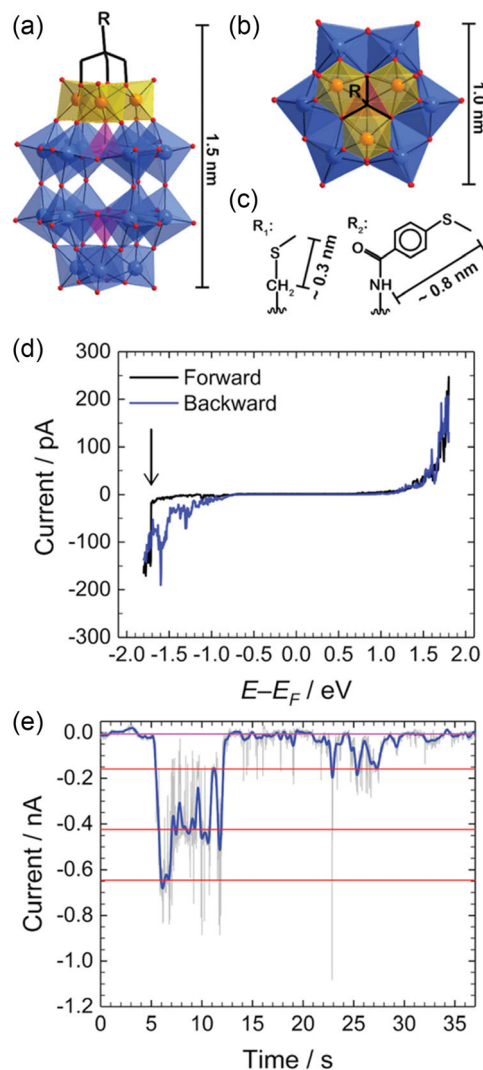


Figure 9. The (OCH₂)₃C-R ligated WD polyoxoanion. a) Side view. b) Top view. c) Ligand scaffolds: R₁ = CH₂SMe of WDS-1 and R₂ = NHCOCH₂SMe of WDS-2. Color code: blue octahedra = WO₆, yellow octahedra = VO₆, magenta square pyramids = PO₄, red spheres = O. H atoms are not shown. d) Switching events of WDS-2 on Au(111). A representative STS spectrum ($I_T = 200$ pA, $U_B = 1.8$ V). In the forward direction (black), the switching from a high-resistive state to a low-resistive state at -1.7 V is clearly discernible. e) Time-resolved resistive switching of WDS-2. A background subtracted $I-t$ spectrum is shown. Three conductivity levels are emphasized by red lines ($I_T = 200$ pA, $U_B = -1.8$ V). Adapted with permission.^[47] Copyright © 2022, John Wiley & Sons.

dissipation due to thinner electrodes might contribute to the observed switching behavior. The limited current provided by most c-AFM amplifiers may also be insufficient to migrate enough V_O , affecting the occurrence of BS. Variations in operating voltage and uniformity are influenced by size-dependent nanocrystal structural changes, with smaller BZO and SZO NPs likely having higher lattice parameters. The Tauc method applied to UV-vis absorption spectra shows a red shift in the bandgaps of both BZO and SZO systems with decreasing NP diameter, which is attributed to increased V_O concentration in smaller diameter NPs, leading to lower V_{SET} and improved switching uniformity. The authors again assumed that the I - V responses of the BZO-SZO combinations reveal that the underlying mechanism driving current in ligand-capped NP assemblies strongly depends on ligand length. Longer organic ligands, e.g., 2-[2-(2-methoxyethoxy)ethoxy]acetic acid, result in charge transport limited current, while shorter ligands, such as 2-hexyldecylphosphonic acid, lead to charge injection limited systems. The switching mechanism thereby involves charge trap/detrapping cycles at the tip-sample interface facilitated by interfacial V_O electron traps.

A first step toward integration by realizing a device-like set-up was achieved by immobilizing sub-10 nm rod like and spherical tri-*n*-octylphosphineoxide-stabilized HfO_2 NPs (TOPO- HfO_2 -NP) in lithographically fabricated electrode structures.^[45]

The NC were drop-casted in dense films onto either micro-channel devices or nanoelectrode structures (see **Figure 8**).

In the nanoelectrode configuration, the Au/TOPO- HfO_2 /Au structures included only a few NPs embedded between the two electrode tips. It was shown that even traces of residual moisture in the atmosphere lead to redox-like behavior that accords to water splitting reactions, whereas under vacuum, for either the microchannel devices and the nanogap devices showed threshold switching. It was hypothesized that the applied voltage induces a polarization in the dry NP hybrid material, which aligns contrary to the electric field, contributing to a self-limited current. The polarization could be due to surplus nonadsorbed TOPO molecules, dipoles at the TOPO/metal interfaces, or within the dry NP itself, which may reorient under an electric field, especially with charge injection from the electrodes or redistribution of surface charges. If the electric field decreases below a certain level, the polarization disappears, making the dry NP film behave like a

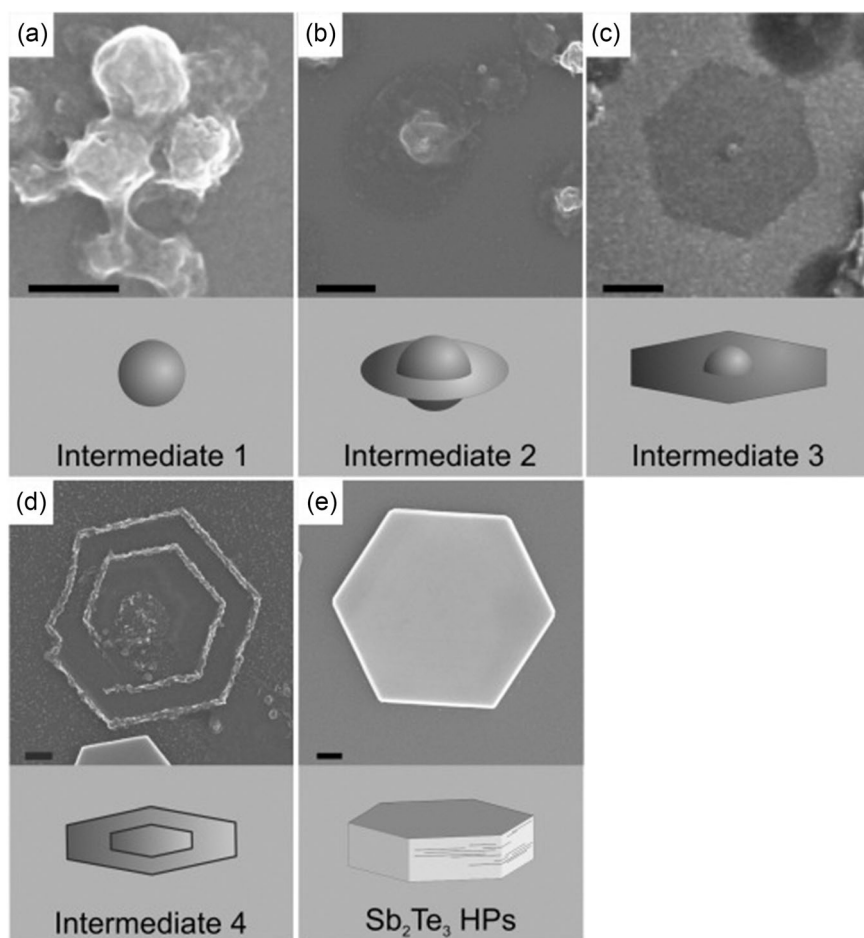


Figure 10. Series of SEM images of intermediates identified during the solvothermal synthesis of Sb_2Te_3 and corresponding simplified models that illustrate the respective morphologies. a) Intermediate 1, amorphous spherical Sb_xTe_y particles, b) Intermediate 2, “fried egg” like structure, c) Intermediate 3, evolution of a hexagonal shape, d) Intermediate 4, hexagonally shaped layers with convex rim, e) final Sb_2Te_3 hexagonal platelets. Scale bar: 200 nm. Reproduced with permission^[61] Copyright © 2015 WILEY-VCH Verlag GmbH & Co. KGaA, Weinheim.

dielectric or poor semiconductor. This means that the volatile threshold switching observed for TOPO-stabilized HfO_2 NPs, tested without moisture, represents the combined properties of the dry NP film and the device design, rather than the NP alone, which highlights the importance of the capping ligands depending on the device architecture.

Approaching the hypothetical size limit of oxide NPs, i.e., clusters that consist of less than 100 atoms (excluding the organic ligand shell), a very recent approach demonstrated the synthesis of two types of so-called Wells–Dawson polyoxoanions ($(\text{tBu}_4\text{N})_5[\text{HP}_2\text{V}_3\text{W}_{15}\text{O}_{59}((\text{OCH}_2)_3\text{C-R})]$) (see Figure 9a–c).^[46,47] The two different polyoxoanions differ only in the composition of the surface-bound ligands R, i.e., $\text{R}_1 = \text{CH}_2\text{SMe}$ or $\text{R}_2 = \text{NHCOC}_6\text{H}_4\text{SMe}$ (WDS-2) and were studied toward their RS behavior on a gold surface. It was found that the type of ligand used in these polyoxoanions affected how they assembled at the surface: WDS-2, with a longer ligand R_2 , formed larger uniform structures while WDS-1, with a shorter ligand R_1 , created smaller agglomerates and thus enables the potential of directed assembly of these polyoxo species.

More relevant regarding this Review, a connection between these polyoxoanions' electronic structures and their interactions with the gold surface could be demonstrated, which impacts their redox state. The experiments were conducted by means of a two-terminal memory cell test structure within a scanning tunneling microscope and by scanning tunneling spectroscopy. The vanadium centers within both WDS-1 and WDS-2 were reduced when in direct contact with the gold surface, resulting in a decreased bandgap. This reduction was interpreted as RS of the polyoxoanions. Notably, the discovery that was made here describes a switching procedure that is controlled by the vanadium centers in these polyoxoanions, independent of the ligand type, which demonstrates the theoretical feasibility of using polyoxoanions in ReRAM devices.

3. Metal Chalcogenide Nanoparticles in Phase Change Settings

3.1. Electrical Addressing of Individual Nanoparticles

There are many metal chalcogenides (consisting of, e.g., Ge, Sb(Bi), Te) known in binary, ternary, and quasi-binary compositions that have applicability in PC memory devices.^[48] Nowadays, these materials are widely used in forms of polycrystalline or amorphous thin films made by gas-phase deposition techniques like sputtering.^[49] Thin films are also being produced by metal-organic chemical vapor deposition (MOCVD) and epitaxial growth depositions with the advantage of highly ordered single crystal structures.^[50] By sputtering different thin films, for example Bi_xTe_y , it was found that depending on small deviations of the favored stoichiometry (Bi_2Te_3), huge property contrasts in terms of thermal and electrical conductivity occurs.^[51,52] This leads to further investigation in wet-chemical syntheses of three-dimensionally confined nanoparticulate materials for there is a great interest on getting insights on the formation of exact compositions in these three-dimensionally (3D) confined materials.^[53]

A challenge in working with PC materials (PCM) is their high tendency to form oxides which makes the oxygen-free handling

unavoidable.^[54] Even though, for the binary PCM GeTe studies showed that small amounts of oxygen doping can enhance the thermal stability of the amorphous phase just slightly higher oxygen quantities lead to the failure of RS properties.^[55] Therefore, the air-free syntheses and transport of PCM into optically and electrically addressable matrices shows ground for investigation.^[56] Furthermore, problems in studying NPs arise when these need to be stabilized by organic ligands which might influence the switching behavior.^[45]

Antimony telluride (Sb_2Te_3) as a narrow bandgap semiconductor has been investigated thoroughly over the years in form of nanoscaled single crystalline and polycrystalline thin layers^[57,58] as it has ever since been of great interest in rewritable optical recording material.^[59] However, layered structures are just confined in one spatial dimension, unless the electrical contacts are truly in nanoscale dimension. In order to explore the size- and structure-related properties of these materials and to approach the three-dimensionally confined state, in 2015, Saltzmann et al. proposed an environmentally friendly solvothermal way to synthesize single-crystalline Sb_2Te_3 hexagonal platelets (HP) by using precursor oxides in a basic medium.^[60,61]

They analyzed the formation process by stopping the reaction at different reaction times and characterized each intermediate starting from an amorphous NP structures (see Intermediate 1 and 2 in Figure 10) to partially crystalline and eventually single crystal Sb_2Te_3 HP (Intermediates 3 and 4 see Figure 10, respectively). In the intermediate states 1–3, the material showed stoichiometries that differed from the ideal Sb_2Te_3 stoichiometry and only after the final structure was achieved the particle can be considered a typical PCM.^[62] First, electrical switching

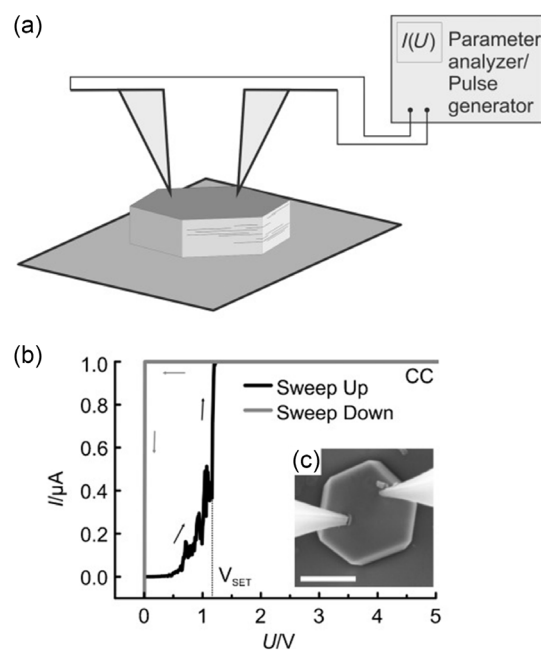


Figure 11. a) Nanorobotic measuring setup in the SEM. b) Switching sweep measured for an in situ contacted Sb_2Te_3 hexagonal platelet in the SEM. c) Positions of the measuring tips during measurement the switching events. Scale bar: 1 μm . Reproduced with permission^[61] Copyright © 2015 WILEY-VCH Verlag GmbH & Co. KGaA, Weinheim.

experiments were performed in an in situ-nanorobotic setup integrated in an SEM, as it was already described above.^[33] Individual NPs were contacted by two metal-coated AFM tips and probed with a switching sweep between 0 V and 5 V after a short amorphization pulse, where typical unipolar switching characteristics between a high and low resistive state were observed (**Figure 11**). After a few cycles, the material showed no switching behavior anymore and stayed in the LRS. The authors assumed that the loss of tellurium and therefore a non-ideal stoichiometry due to the experimental setup in vacuum caused this loss in functionality.

Nevertheless, this first RS experiments on individual particles set the ground for further experiments.^[32,63,64] In 2018, Jacobs-Gedrim et al. showed RS in 2D confined Sb_2Te_3 nanoflakes formed by exfoliation processes. Here, the particles were placed between two Ti/Au metal contacts and could successfully be

switched over more than 20 cycles between HRS and LRS. They also found that the energy required to amorphize the crystalline material decreases exponentially with thickness reduction.^[65,66] Comparing the thickness of the wet-chemically synthesized Sb_2Te_3 HP with roughly 200 nm and the exfoliated nanoflakes of 20–100 nm the confinement into two dimensions seems to increase the stability of the elemental composition during switching processes.

In order to advance the understanding of this particular PCM and its role in RS, a comparison was drawn between Sb_2Te_3 structures formed by molecular beam epitaxy (MBE) and those synthesized chemically. Their optical properties were scrutinized using scattering-type scanning nearfield optical microscopy (s-SNOM).^[67] This method, with its 20 nm resolution, facilitated a detailed exploration of individual particles (**Figure 12**). A distinct optical contrast was found within different surface

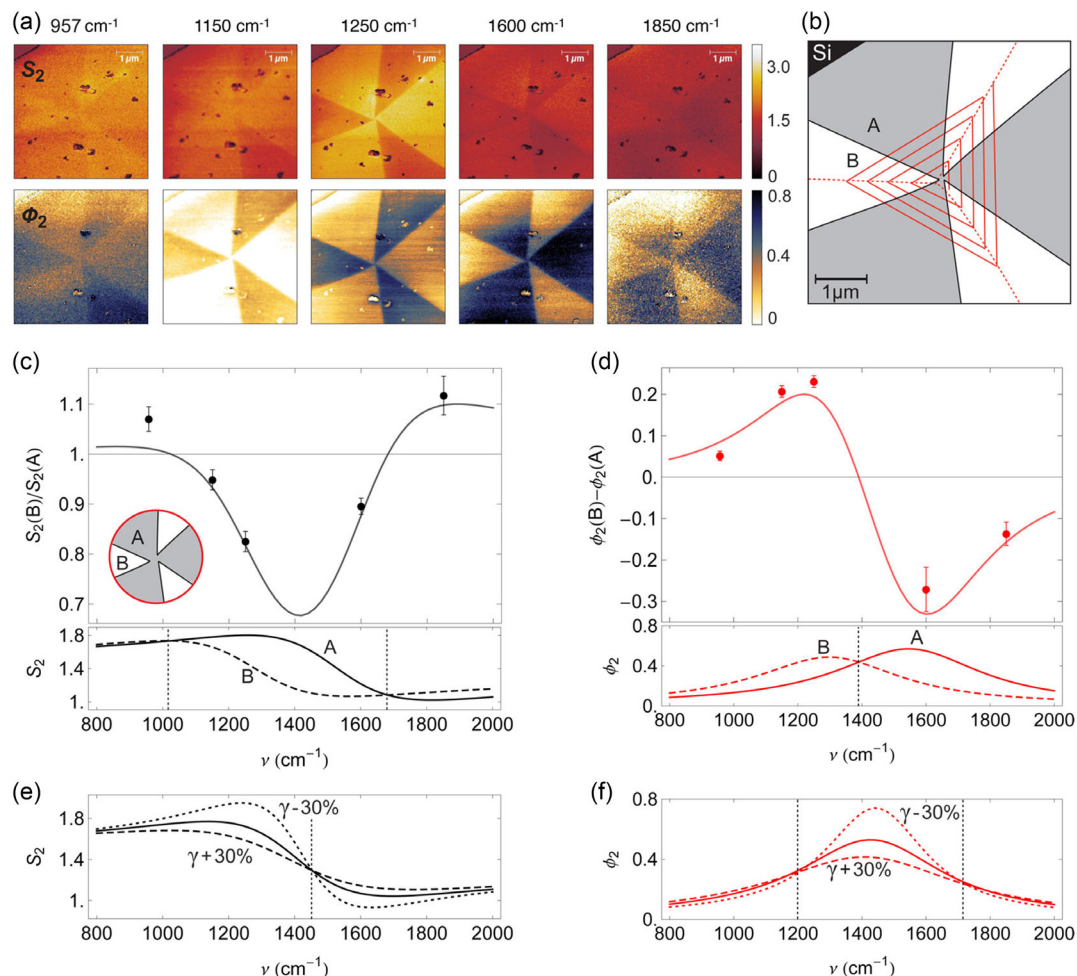


Figure 12. (a) Near-field optical images in scattering amplitude S_2 (first row) and phase ϕ_2 (second row), normalized to silicon (upper left corner). The five columns show measurements for different illumination frequencies. A schematic overlay of the optical pattern from a) with the topography of the growth spiral is shown in b). In c) and d), the relative contrast between the domains, as labeled in b), is plotted in amplitude and phase, respectively. In the inset of c), the area of 500 nm radius around the screw dislocation that is used for the evaluation of the relative contrasts is sketched. The lines are calculated near-field contrasts under the assumption of different Drude terms for the domains A and B: $N_A = 2.1 \cdot 10^{20} \text{ cm}^{-3}$, $N_B = 1.5 \cdot 10^{20} \text{ cm}^{-3}$. In the lower plots, the respective contrast to silicon is shown. e) and f) Illustrations of the effect of a variation of $\pm 30\%$ around the extracted damping factor $\gamma = 540 \text{ cm}^{-1}$ while N is kept constant at $1.8 \cdot 10^{20} \text{ cm}^{-3}$. Crossing points which indicate an inversion of the contrast between two spectra are marked with vertical dashed lines. Reproduced with permission.^[67] Copyright © 2015 American Chemical Society.

segments of a single particle, attributable to variations in charge carrier densities resulting from slight Sb:Te ratio discrepancies on the particle surface. Such variations are essential when it comes to conductivity changes and are thereby central to RS in PCMs in general.

Conventional AFM experiments confirmed a spiral growth pattern on the Sb_2Te_3 surface, as previously identified by Saltzmann et al. (see Figure 10d).^[61] This pattern was observed to occasionally cause contrast inversion. Upon adjusting the supersaturation of growth species, symmetric infrared domains emerged as an inherent trait of Sb_2Te_3 . This observation held true for both chemically synthesized particles and MBE-produced nanofilms.^[68]

These few examples show that metal chalcogenide NPs can in principle be applicable in RS settings. However, in contrast to metal oxides, they are less stable in terms of stoichiometric integrity during switching experiments. Furthermore, it is evident that the particles studied so far still reach up to the micrometer range in at least one lateral dimension. Hence, the features of a three-dimensional (3D) confinement have not yet been explored, as only a few PCM in (true) NP form have been synthesized so far. To the best of our knowledge, on such NP systems, electrical switching experiments have not been published yet. However, as detailed structural investigation on the structural features and the stability of the amorphous state as a function of particle size have been performed, we include examples from those studies in this review, as they shed light in the potential of chemical design also for RS purposes.

3.2. Stabilizing Amorphous GeTe by 3D Confinement

The group of Yarema did pioneering work on analyzing the 3D confinement effect in PCM on the phase stability and transition

between the amorphous and crystalline state.^[69] They showed a wet-chemical synthesis approach to achieve ligand stabilized GeTe NPs in a variety of sizes between 4 and 8 nm in diameter and thereby enabled the analysis of the size-dependent crystallization temperature (T_c). Previous synthesis of amorphous GeTe NPs in a nonsize-controllable manner showed already that decreasing size from bulk to a particle size diameter of 1.8 nm leads to a drastic increase in crystallization temperature from $T_c = 170^\circ\text{C}$ to $T_c = 400^\circ\text{C}$.^[70,71]

The investigation by high temperature p-XRD of 6 nm GeTe NP further showed that the crystalline domain size increased up to 25 nm which indicated that the coalescence of the NPs occurs at a similar temperature range as the crystallization. Analyzing the temperature-dependent behavior of 3D confined NPs is even more difficult due to the fact that the size-dependent trends of T_c and of the melting temperature (T_m) are opposite. While T_m is decreasing with decreasing size due to higher energy per atom with increasing number of surface atoms, T_c is increasing. To distinguish between these thermally induced phenomena, differential scanning calorimetry with different heating rates was performed. While the exothermic T_c and the endothermic T_m at high temperatures are clearly distinct from each other during these measurements, the T_c signal is broadened. With higher heating rates, the exothermic signal can be subdivided into two exothermic peaks and are identified as crystallization at lower temperature and coalescence at higher temperature. Therefore, additional in situ-heating transmission electron microscopy (TEM) experiments were conducted. The slightly higher coalescence temperature was explained by the organic ligand shell stabilizing the NPs which causes a physical gap for atomic diffusion and coalescence. This hypothesis was backed up by exchanging the larger organic ligand by inorganic anions which revealed a crystallization of GeTe NPs around $T_c = 170^\circ\text{C}$ which aligns with T_c of bulk

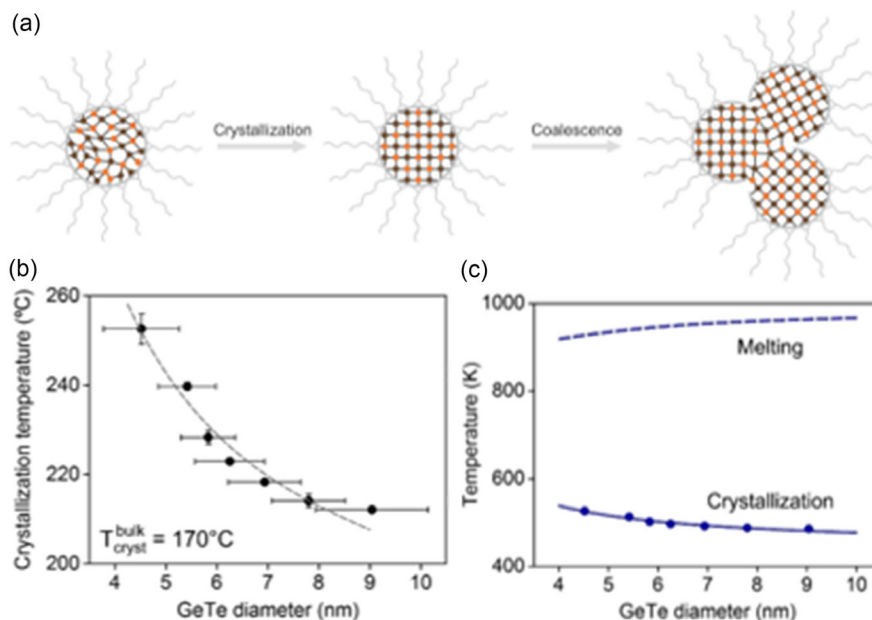


Figure 13. a) Schematic representation of crystallization and coalescence of GeTe NPs, when covered with organic ligands. b) Size dependence of crystallization temperature for GeTe NPs extracted from peak intensity profiles and fitted with entropy of crystallization model. c) Size effects on crystallization and melting. Adapted with permission.^[69] Copyright © 2018 American Chemical Society.

GeTe (see Figure 13c). This might give some insights into the improvement in data retention at room temperature. Also, the power consumption in order to crystallize/melt the GeTe NP can be found on the same level as synaptic events in living organism which opens the fields of ultralow power consumption memory devices by 3D confinement.^[69,72]

The investigation on the optical properties therefore the reflective index, extinction coefficient, and the optical bandgap of amorphous and crystalline GeTe NPs was performed in 2020 by Michel et al. by using spectroscopic ellipsometry.^[73] The inorganic ligand stabilized particles ($\text{GeTe}@I^-$) were spin-coated as thin films onto a Si substrate with a native 100 nm SiO_2 layer. In order to avoid the prone degradation during annealing processes of GeTe, the particle thin layer was then coated with a ≈ 40 nm layer of SiO_2 via sputtering (see Figure 14).^[74]

The sample annealing up to 300 °C leads to the expected crystallization of the particles^[69] and could even be seen visibly by a change of surface color of the substrate and was confirmed by p-XRD. The optical properties of GeTe in bulk are already known^[75–77] and could therefore be nicely compared to the 3D

confined material in a size range of roughly 6 nm. It was found that the GeTe NPs show a smaller reflective index and extinction coefficient and a larger optical bandgap than a sputtered thin layer. This can be attributed to the relatively smaller volume fraction and confinement effect due to size limitation in all dimensions of NPs.^[78] Additionally to binary PCM recently the investigation into M-GeTe NP (described as quantum dots with $M = \text{Sn}$) which showed a decrease of T_c with increasing amount of Sn. Furthermore, a large reflectivity contrast between the crystalline and amorphous material phase was observed.^[79] In conclusion, the investigation on 3D confined PC material NP as well as formation processes and surface engineering could not only increase the access to this material class due to a facilitated fabrication process but also provide a platform to tailor the properties of these materials.

4. Summary and Outlook

We have discussed selected examples of the RS properties of NP, both in assemblies as well as on the individual particle level.

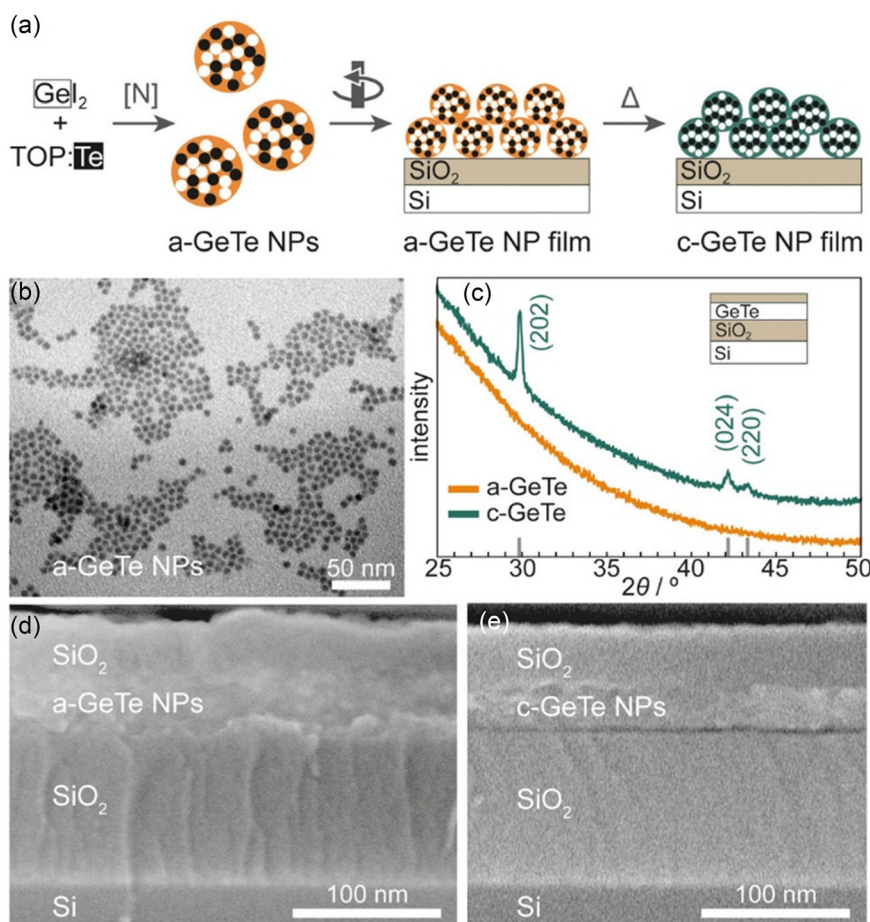


Figure 14. a) After the a-GeTe NPs were synthesized following an amide-promoted route, films were fabricated by spin-coating. Annealing under nitrogen led to crystalline NP-based thin films, indicating partial NP sintering. The atomic arrangement (Ge: black; Te: white) is only a schematic illustration of the structural order and does not represent the atomic lattice. b) TEM image of as-synthesized a-GeTe NPs with an average diameter of 5.8 nm. The a-GeTe and c-GeTe thin film samples were characterized via X-ray diffraction in c) with a scheme of the sample stack in the inset. The peaks are indexed to the rhombohedrally distorted α -phase of c-GeTe (gray ticks according to JCPDS #47–1079). Cross sections of these samples were further characterized via SEM shown in d) and e). Reproduced with permission.^[73] Copyright © 2020 American Chemical Society.

Although this field of research is in a rather premature state, it becomes evident that the versatility of chemical synthesis that allow the tailoring of size, shape, and composition of NPs bears a major potential for RS applications. One of the main challenges will be the integration of individual NP into a nanoelectrode circuitry, but the progress in the studies of individual NP properties, which has been achieved in recent years, holds promise that the effort to be taken for achieving this goal is worthwhile. Thereby the strategies to integrate metal NPs into nanoelectrode configurations may be a good guidance for integration individual VC and PC NPs into nanoelectrode circuitry as well. In comparison to PC NPs, the VC NP properties, typically consisting of metal oxides, are a bit more explored up to now, so that even RS properties have been studied on the single particle level. Additionally, metal oxides suffer less from chemical instabilities, such as phase segregation or demixing, as it is observed in most of the PC materials.

Furthermore, one might anticipate that the field of NP-based RS will benefit from the huge variety of different metal oxide NPs, for which synthesis protocols have already been developed for other purposes.

For PC, the recent discovery of the size-dependent crystallization temperature could be a very promising cornerstone for utilizing this 3D confinement effect for electrical RS applications. However, the challenge of compositional instability under electrical load, predominately by Joule heating and probably by differences in ion migration,^[21] might be overcome by reducing the compositional complexity, e.g., by synthesizing monometallic NP that may promise higher stability. This concept may be deduced from the work of Salina et al. who applied pure antimony for optical PC studies. They showed that sub-10 nm layers of crystalline Sb could successfully be amorphized and stabilized up to 50 h at room temperature, which goes well beyond the properties of bulk Sb, which cannot be stabilized in its metastable amorphous state.^[80] This example as well as very recent studies on mechanism of amorphous phase stabilization in ultrathin films^[81] may be inspiring for chemists and materials scientists to develop synthesis routes for sub-10 nm Sb NP and well as of other metalloids that hold promise for higher cycle stability.

Acknowledgements

A.F. and T.O. contributed equally to this work. This work has been funded by Deutsche Forschungsgemeinschaft (DFG) through SFB 917 "Nanoswitches".

Open Access funding enabled and organized by Projekt DEAL.

Conflict of Interest

The authors declare no conflict of interest.

Keywords

chalcogenides, metal oxides, nanoparticles, resistive switching

Received: June 19, 2023

Revised: July 20, 2023

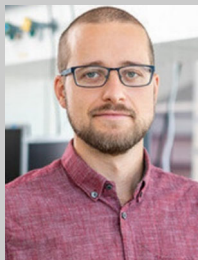
Published online:

- [1] A. Barhoum, M. L. Garcia-Betancourt, J. Jeevanandam, E. A. Hussien, S. A. Mekawy, M. Mostafa, M. M. Omran, S. Abdalla, M. Bechelany, *Nanomaterials* **2022**, *12*, 177.
- [2] J. A. Darr, J. Zhang, N. M. Makwana, X. Weng, *Chem. Rev.* **2017**, *117*, 11125.
- [3] H. Kim, S. Beack, S. Han, M. Shin, T. Lee, Y. Park, K. S. Kim, A. K. Yetisen, S. H. Yun, W. Kwon, S. K. Hahn, *Adv. Mater.* **2018**, *30*, 1701460.
- [4] S. Fan, J. Li, H.-Q. Cao, X. Liu, M. Cao, T. Liu, T. Xu, J. Su, *J. Mater. Chem. C* **2022**, *10*, 14053.
- [5] M. Parashar, V. K. Shukla, R. Singh, *J. Mater. Sci.* **2020**, *31*, 3729.
- [6] A. K. Pearce, T. R. Wilks, M. C. Arno, R. K. O'Reilly, *Nat. Rev. Chem.* **2021**, *5*, 21.
- [7] L. Scarabelli, M. Sun, X. Zhuo, S. Yoo, J. E. Millstone, M. R. Jones, L. M. Liz-Marzan, *Chem. Rev.* **2023**, *123*, 3493.
- [8] D. V. Talapin, E. V. Shevchenko, *Chem. Rev.* **2016**, *116*, 10343.
- [9] J. Wang, Z. Wang, W. Wang, Y. Wang, X. Hu, J. Liu, X. Gong, W. Miao, L. Ding, X. Li, J. Tang, *Nanoscale* **2022**, *14*, 6709.
- [10] M. E. Franke, T. J. Koplin, U. Simon, *Small* **2006**, *2*, 36.
- [11] H. W. Tan, J. An, C. K. Chua, T. Tran, *Adv. Electron. Mater.* **2019**, *5*, 1800831.
- [12] P. Z. Zhang, L. L. Liang, X. G. Liu, *J. Mater. Chem. C* **2021**, *9*, 16110.
- [13] Y. Q. Wang, S. A. Skaavik, X. Y. Xiong, S. Y. Wang, M. D. Dong, *Matter* **2021**, *4*, 3483.
- [14] S. Karthäuser, S. Peter, U. Simon, *Eur. J. Inorg. Chem.* **2020**, *2020*, 3798.
- [15] M. Mennicken, S. K. Peter, C. Kaulen, U. Simon, S. Karthäuser, *Beilstein J. Nanotechnol.* **2022**, *13*, 219.
- [16] *Nanoelectronics and Information Technology* (Ed: R. Waser), 3rd ed., Wiley-VCH, Berlin **2012**.
- [17] W. Banerjee, A. Kashir, S. Kamba, *Small* **2022**, *18*, e2107575.
- [18] E. Carlos, R. Branquinho, R. Martins, A. Kiazadeh, E. Fortunato, *Adv. Mater.* **2021**, *33*, e2004328.
- [19] R. Dittmann, S. Menzel, R. Waser, *Adv. Phys.* **2022**, *70*, 155.
- [20] W. Zhang, R. Mazzarello, M. Wuttig, E. Ma, *Nat. Rev. Mater.* **2019**, *4*, 150.
- [21] Y. Xu, Y. Zhou, X. D. Wang, W. Zhang, E. Ma, V. L. Deringer, R. Mazzarello, *Adv. Mater.* **2022**, *34*, e2109139.
- [22] T. H. Kim, E. Y. Jang, N. J. Lee, D. J. Choi, K. J. Lee, J. T. Jang, J. S. Choi, S. H. Moon, J. Cheon, *Nano Lett.* **2009**, *9*, 2229.
- [23] Q. Hu, S. M. Jung, H. H. Lee, Y.-S. Kim, Y. J. Choi, D.-H. Kang, K.-B. Kim, T.-S. Yoon, *J. Phys. D: Appl. Phys.* **2011**, *44*, 085403.
- [24] J.-D. Kim, Y.-J. Baek, Y. Jin Choi, C. Jung Kang, H. Ho Lee, H.-M. Kim, K.-B. Kim, T.-S. Yoon, *J. Appl. Phys.* **2013**, *114*, 224505.
- [25] H. Schroeder, *J. Appl. Phys.* **2015**, *117*, 215103.
- [26] R. Waser, R. Dittmann, G. Staikov, K. Szot, *Adv. Mater.* **2009**, *21*, 2632.
- [27] M. Zhao, B. Gao, J. Tang, H. Qian, H. Wu, *Appl. Phys. Rev.* **2020**, *7*, 011301.
- [28] A. Younis, D. Chu, I. Mihail, S. Li, *ACS Appl. Mater. Interfaces* **2013**, *5*, 9429.
- [29] Z. Ahmadi, H. Lu, P. Mukherjee, M. Koten, A. Gruverman, J. E. Shield, *Adv. Electron. Mater.* **2020**, *6*, 2000065.
- [30] D. Ielmini, C. Cagli, F. Nardi, Y. Zhang, *J. Phys. D: Appl. Phys.* **2013**, *46*, 074006.
- [31] C. Cagli, F. Nardi, B. Harteneck, Z. Tan, Y. Zhang, D. Ielmini, *Small* **2011**, *7*, 2899.
- [32] D. O. Schmidt, S. Hoffmann-Eifert, H. Zhang, C. La Torre, A. Besmehn, M. Noyong, R. Waser, U. Simon, *Small* **2015**, *11*, 6444.
- [33] M. Noyong, K. Blech, A. Rosenberger, V. Klocke, U. Simon, *Meas. Sci. Technol.* **2007**, *18*, N84.
- [34] D. O. Schmidt, N. Raab, M. Noyong, V. Santhanam, R. Dittmann, U. Simon, *Nanomaterials* **2017**, *7*, 370.
- [35] N. Schmidt, K. Z. Rushchanskii, U. Trstenjak, R. Dittmann, S. Karthäuser, *ACS Appl. Nano Mater.* **2022**, *6*, 148.

- [36] W. P. Lin, S. J. Liu, T. Gong, Q. Zhao, W. Huang, *Adv. Mater.* **2014**, 26, 570.
- [37] G. U. Siddiqui, M. M. Rehman, Y.-J. Yang, K. H. Choi, *J. Mater. Chem. C* **2017**, 5, 862.
- [38] J.-W. Lee, W.-J. Cho, *Semicond. Sci. Technol.* **2017**, 32, 025009.
- [39] N. K. Pham, N. H. Vu, V. V. Pham, H. K. T. Ta, T. M. Cao, N. Thoai, V. C. Tran, *J. Mater. Chem. C* **2018**, 6, 1971.
- [40] H. H. Nguyen, H. K. T. Ta, S. Park, T. B. Phan, N. K. Pham, *RSC Adv.* **2020**, 10, 12900.
- [41] K. Krishnan, M. Aono, K. Terabe, T. Tsuruoka, *J. Phys. D: Appl. Phys.* **2019**, 52, 445301.
- [42] J. Wang, S. Choudhary, J. De Roo, K. De Keukeleere, I. Van Driessche, A. J. Crosby, S. S. Nonnenmann, *ACS Appl. Mater. Interface* **2018**, 10, 4824.
- [43] S. H. Chang, S. C. Chae, S. B. Lee, C. Liu, T. W. Noh, J. S. Lee, B. Kahng, J. H. Jang, M. Y. Kim, D. W. Kim, C. U. Jung, *Appl. Phys. Lett.* **2008**, 92, 183507.
- [44] Y. C. Yang, F. Pan, F. Zeng, *New J. Phys.* **2010**, 12, 023008.
- [45] S. Maiti, T. Ohlerth, N. Schmidt, S. Aussen, R. Waser, U. Simon, S. Karthäuser, *J. Phys. Chem. C* **2022**, 126, 18571.
- [46] M. Globeta, R. Putt, M. Moors, E. Kentzinger, W. Pyckhout-Hintzen, K. Y. Monakhov, *Nanoscale* **2019**, 11, 4267.
- [47] M. Glöß, R. Pütt, M. Moors, E. Kentzinger, S. Karthäuser, K. Y. Monakhov, *Adv. Mater. Interfaces* **2022**, 9, 2270117.
- [48] M. Wuttig, N. Yamada, *Nat. Mater.* **2007**, 6, 824.
- [49] F. Amirghasemi, S. Kassegne, *J. Electron. Mater.* **2021**, 50, 2190.
- [50] P. D. Szkutnik, M. Aoukar, V. Todorova, L. Angélics, B. Pelissier, D. Jourde, P. Michallon, C. Vallée, P. Noé, *J. Appl. Phys.* **2017**, 121, 105301.
- [51] M. Goto, M. Sasaki, Y. B. Xu, T. Z. Zhan, Y. Isoda, Y. Shinohara, *Appl. Surf. Sci.* **2017**, 407, 405.
- [52] Y.-J. Wu, S.-C. Hsu, Y.-C. Lin, Y. Xu, T.-H. Chuang, S.-C. Chen, *Surf. Coat. Technol.* **2020**, 394, 125694.
- [53] B. J. Kooi, M. Wuttig, *Adv. Mater.* **2020**, 32, e1908302.
- [54] R. Golovchak, Y. G. Choi, S. Kozlyukhin, Y. Chigirinsky, A. Kovalskiy, P. Xiong-Skiba, J. Trimble, R. Pafchek, H. Jain, *Appl. Surf. Sci.* **2015**, 332, 533.
- [55] X. Zhou, Y. Du, J. K. Behera, L. Wu, Z. Song, R. E. Simpson, *ACS Appl. Mater. Interface* **2016**, 8, 20185.
- [56] R. J. Hermann, M. J. Gordon, *Annu. Rev. Chem. Biomol. Eng.* **2018**, 9, 365.
- [57] D. Gu, D. Nminibapiel, H. Baumgart, H. Robinson, V. Kochergin, *ECS Trans.* **2011**, 41, 255.
- [58] J. Yadav, R. Singh, M. D. Anoop, N. Yadav, N. Srinivasa Rao, F. Singh, K. Awasthi, M. Kumar, *Mater. Lett. X* **2021**, 12, 100113.
- [59] R. S. Rawat, P. Arun, A. G. Vedeshwar, Y. L. Lam, M. H. Liu, P. Lee, S. Lee, A. C. H. Huan, *Mater. Res. Bull.* **2000**, 35, 477.
- [60] H. J. Im, B. Koo, M. S. Kim, J. E. Lee, *Appl. Surf. Sci.* **2019**, 475, 510.
- [61] T. Saltzmann, M. Bornhoff, J. Mayer, U. Simon, *Angew. Chem. Int. Ed.* **2015**, 54, 6632.
- [62] T. Saltzmann, *PhD Thesis*, RWTH Aachen University (Aachen) **2014**.
- [63] M. Hosseini, N. Frick, D. Guilbaud, M. Gao, T. H. LaBean, *J. Vac. Sci. Technol. B* **2022**, 40, 043201.
- [64] S.-H. Lee, D.-K. Ko, Y. Jung, R. Agarwal, *Appl. Phys. Lett.* **2006**, 89, 223116.
- [65] R. B. Jacobs-Gedrim, M. T. Murphy, F. Yang, N. Jain, M. Shanmugam, E. S. Song, Y. Kandel, P. Hesamaddin, H. Y. Yu, M. P. Anantram, D. B. Janes, B. Yu, *Appl. Phys. Lett.* **2018**, 112.
- [66] F. Yang, R. B. Jacobs-Gedrim, M. Shanmugam, N. Jain, M. T. Murphy, E. S. Song, D. Frey, B. Yu, *RSC Adv.* **2015**, 5, 59320.
- [67] B. Hauer, T. Saltzmann, U. Simon, T. Taubner, *Nano Lett.* **2015**, 15, 2787.
- [68] M. Lewin, L. Mester, T. Saltzmann, S.-J. Chong, M. Kaminski, B. Hauer, M. Pohlmann, A. M. Mio, M. Wirtsohn, P. Jost, M. Wuttig, U. Simon, T. Taubner, *ACS Appl. Nano Mater.* **2018**, 1, 6834.
- [69] O. Yarema, A. Perevedentsev, V. Ovuka, P. Baade, S. Volk, V. Wood, M. Yarema, *Chem. Mater.* **2018**, 30, 6134.
- [70] I. U. Arachchige, R. Soriano, C. D. Malliakas, S. A. Ivanov, M. C. Kanatzidis, *Adv. Funct. Mater.* **2011**, 21, 2737.
- [71] M. A. Caldwell, S. Raoux, R. Y. Wang, H. S. Philip Wong, D. J. Milliron, *J. Mater. Chem.* **2010**, 20, 1285.
- [72] W. Xu, S. Y. Min, H. Hwang, T. W. Lee, *Sci. Adv.* **2016**, 2, e1501326.
- [73] A. K. U. Michel, M. Sousa, M. Yarema, O. Yarema, V. Ovuka, N. Lassaline, V. Wood, D. J. Norris, *ACS Appl. Nano Mater.* **2020**, 3, 4314.
- [74] A. N. D. Kolb, N. Bernier, E. Robin, A. Benayad, J.-L. Rouvière, C. Sabbione, F. Hippert, P. Noé, *ACS Appl. Electron. Mater.* **2019**, 1, 701.
- [75] J.-W. Park, S. H. Eom, H. Lee, J. L. F. Da Silva, Y.-S. Kang, T.-Y. Lee, Y. H. Khang, *Phys. Rev. B* **2009**, 80, 115209.
- [76] J. W. Park, S. H. Baek, T. D. Kang, H. Lee, Y. S. Kang, T. Y. Lee, D. S. Suh, K. J. Kim, C. K. Kim, Y. H. Khang, J. L. F. Da Silva, S. H. Wei, *Appl. Phys. Lett.* **2008**, 93, 021914.
- [77] K. Shportko, S. Kremers, M. Woda, D. Lencer, J. Robertson, M. Wuttig, *Nat. Mater.* **2008**, 7, 653.
- [78] S. Furukawa, T. Miyasato, *Phys. Rev. B* **1988**, 38, 5726.
- [79] D. Kumaar, M. Can, K. Portner, H. Weigand, O. Yarema, S. Wintersteller, F. Schenk, D. Boskovic, N. Pharizat, R. Meinert, E. Gilshtein, Y. Romanyuk, A. Karvounis, R. Grange, A. Emboras, V. Wood, M. Yarema, *ACS Nano* **2023**, 17, 6985.
- [80] M. Salinga, B. Kersting, I. Ronneberger, V. P. Jonnalagadda, X. T. Vu, M. Le Gallo, I. Giannopoulos, O. Cojocaru-Miredin, R. Mazzarello, A. Sebastian, *Nat. Mater.* **2018**, 17, 681.
- [81] D. Dragoni, J. Behler, M. Bernasconi, *Nanoscale* **2021**, 13, 16146.
- [82] Z. Zhou, P. Lopez-Dominguez, M. Abdullah, D. M. Barber, X. Meng, J. Park, I. Van Driessche, J. D. Schiffman, A. J. Crosby, K. R. Kittilstved, S. S. Nonnenmann, *ACS Appl. Mater. Interface* **2021**, 13, 21635.



Anne Frommelius is currently working on her Ph.D. in the research group of Professor Ulrich Simon. She received her Master's degree at the Heinrich-Heine University, Düsseldorf where she was supervised externally from the RWTH Aachen on her Master thesis already by Professor Ulrich Simon, where her interest in the research of nanoparticulate phase change material nanoparticles started.



Thorsten Ohlerth received his Master's degree at the RWTH Aachen University and is currently working on his Ph.D. in the research group of Professor Ulrich Simon. His research interests include the synthesis and characterization of metal oxide nanoparticles.



Michael Noyong is senior scientist in the research group of Professor Ulrich Simon at the Institute of Inorganic Chemistry at RWTH Aachen University in Germany. Born and raised in Essen, Germany, and studied Chemistry at the University of Essen. He gained the doctoral degree at the RWTH Aachen University focusing on DNA-nanoparticle hybrids.



Ulrich Simon currently holds a Full Professorship and Chair at the Institute of Inorganic Chemistry at RWTH Aachen University in Germany. He was born and raised in Essen, Germany. He studied Chemistry at the University of Essen, where he also undertook his doctoral research in solid state chemistry. Since 2000 he has been Professor at the RWTH Aachen University. His research program is focused on the electrofunctional and biofunctional properties of chemically designed nanostructures.